Research Article | Vol. 26, No. 9 | 30 Apr 2018 | OPTICS EXPRESS 11161

Optics EXPRESS

High-Q-factor Al_2O_3 micro-trench cavities integrated with silicon nitride waveguides on silicon

Zhan Su,[1,2,6] Nanxi Li,[1,3] Henry C. Frankis,[4] E. Salih Magden,[1] Thomas N. Adam,[5] Gerald Leake,[5] Douglas Coolbaugh,[5] Jonathan D. B. Bradley,[4,*] and Michael R. Watts[1]

[1]*Photonic Microsystems Group, Research Laboratory of Electronics, Massachusetts Institute of Technology, 77 Massachusetts Avenue, Cambridge, MA 02138, USA*
[2]*Current Affiliation: Analog Photonics, 1 Marina Park Drive, Suite 205, Boston, MA 02210, USA*
[3]*John A. Paulson School of Engineering and Applied Sciences, Harvard University, 29 Oxford Street, Cambridge, MA 02138, USA*
[4]*Department of Engineering Physics, McMaster University, 1280 Main Street West, Hamilton, ON L8S 4L7, Canada*
[5]*Colleges of Nanoscale Science and Engineering, State University of New York Polytechnic Institute, 257 Fuller Road, Albany, NY 12203, USA*
[6]*zhan@analogphotonics.com*
[*]*jbradley@mcmaster.ca*

Abstract: We report on the design and performance of high-Q integrated optical micro-trench cavities on silicon. The microcavities are co-integrated with silicon nitride bus waveguides and fabricated using wafer-scale silicon-photonics-compatible processing steps. The amorphous aluminum oxide resonator material is deposited via sputtering in a single straightforward post-processing step. We examine the theoretical and experimental optical properties of the aluminum oxide micro-trench cavities for different bend radii, film thicknesses and near-infrared wavelengths and demonstrate experimental Q factors of > 10^6. We propose that this high-Q micro-trench cavity design can be applied to incorporate a wide variety of novel microcavity materials, including rare-earth-doped films for microlasers, into wafer-scale silicon photonics platforms.

© 2018 Optical Society of America under the terms of the OSA Open Access Publishing Agreement

OCIS codes: (130.0130) Integrated optics; (140.3948) Microcavity devices; (230.3990) Micro-optical devices; (230.5750) Resonators.

References and links

1. K. J. Vahala, "Optical microcavities," Nature **424**(6950), 839–846 (2003).
2. G. C. Righini, Y. Dumeige, P. Féron, M. Ferrari, G. Nunzi Conti, D. Ristic, and S. Soria, "Whispering gallery mode microresonators: Fundamentals and applications," Riv. Nuovo Cim. **34**(7), 435–488 (2011).
3. H.-Z. Song, "Microcavities for silica-fiber-based quantum information processing," in *Optoelectronics – Advanced Device Structures*, S. L. Pyshkin and J. Ballato, eds. (InTech, 2017).
4. T. J. Kippenberg, R. Holzwarth, and S. A. Diddams, "Microresonator-based optical frequency combs," Science **332**(6029), 555–559 (2011).
5. M. R. Foreman, J. D. Swaim, and F. Vollmer, "Whispering gallery mode sensors," Adv. Opt. Photonics **7**(2), 168–240 (2015).
6. L. He, S. Kaya Özdemir, and L. Yang, "Whispering gallery microcavity lasers," Laser Photonics Rev. **7**(1), 60–82 (2013).
7. W. Bogaerts, P. De Heyn, T. Van Vaerenbergh, K. De Vos, S. K. Selvaraja, T. Claes, P. Dumon, P. Bienstman, D. V. Thourhout, and R. Baets, "Silicon microring resonators," Laser Photonics Rev. **6**(1), 47–73 (2012).
8. A. Biberman, M. J. Shaw, E. Timurdogan, J. B. Wright, and M. R. Watts, "Ultralow-loss silicon ring resonators," Opt. Lett. **37**(20), 4236–4238 (2012).
9. J. F. Bauters, M. J. R. Heck, D. John, D. Dai, M.-C. Tien, J. S. Barton, A. Leinse, R. G. Heideman, D. J. Blumenthal, and J. E. Bowers, "Ultra-low-loss high-aspect-ratio Si_3N_4 waveguides," Opt. Express **19**(4), 3163–3174 (2011).
10. D. J. Moss, R. Morandotti, A. L. Gaeta, and M. Lipson, "New CMOS-compatible platforms based on silicon nitride and Hydex for nonlinear optics," Nat. Photonics **7**(8), 597–607 (2013).

#321169 https://doi.org/10.1364/OE.26.011161
Journal © 2018 Received 31 Jan 2018; revised 27 Mar 2018; accepted 3 Apr 2018; published 16 Apr 2018

11. D. K. Armani, T. J. Kippenberg, S. M. Spillane, and K. J. Vahala, "Ultra-high-*Q* toroid microcavity on a chip," Nature **421**(6926), 925–928 (2003).
12. K. Y. Yang, D. Y. Oh, S. H. Lee, and K. J. Vahala, "Ultra-high-Q silica-on-silicon ridge-ring-resonator with an integrated silicon nitride waveguide," in *CLEO: Science and Innovations 2016*, OSA Technical Digest Series (Optical Society of America, 2016), paper JTh4B.7.
13. J. D. B. Bradley, E. S. Hosseini, Z. Purnawirman, Z. Su, T. N. Adam, G. Leake, D. Coolbaugh, and M. R. Watts, "Monolithic erbium- and ytterbium-doped microring lasers on silicon chips," Opt. Express **22**(10), 12226–12237 (2014).
14. Z. Su, J. D. B. Bradley, N. Li, E. S. Magden, Purnawirman, D. Coleman, N. Fahrenkopf, C. Baiocco, T. N. Adam, G. Leake, D. Coolbaugh, D. Vermeulen, and M. R. Watts, "Ultra-compact CMOS-compatible ytterbium microlaser," in *Advanced Photonics 2016, Integrated Photonics Research, Silicon and Nano-Photonics*, OSA Technical Digest Series (Optical Society of America, 2016), paper IW1A.3.
15. Z. Su, N. Li, E. Salih Magden, M. Byrd, P. Purnawirman, T. N. Adam, G. Leake, D. Coolbaugh, J. D. B. Bradley, and M. R. Watts, "Ultra-compact and low-threshold thulium microcavity laser monolithically integrated on silicon," Opt. Lett. **41**(24), 5708–5711 (2016).
16. E. S. Magden, M. Y. Peng, J. D. B. Bradley, G. Leake, D. Coolbaugh, L. A. Kolodziejski, F. X. Kaertner, and M. R. Watts, "Laser frequency stabilization using Pound-Drever-Hall technique with an integrated TiO_2 athermal resonator," in *CLEO: Science and Innovations 2016*, OSA Technical Digest Series (Optical Society of America, 2016), paper Stu1H.3.
17. K. Wörhoff, J. D. B. Bradley, F. Ay, D. Geskus, T. Blauwendraat, and M. Pollnau, "Reliable low-cost fabrication of low-loss Al_2O_3:Er^{3+} waveguides with 5.4-dB optical gain," IEEE J. Quantum Electron. **45**(5), 454–461 (2009).
18. J. Purnawirman, J. Sun, T. N. Adam, G. Leake, D. Coolbaugh, J. D. B. Bradley, E. Shah Hosseini, and M. R. Watts, "C- and L-band erbium-doped waveguide lasers with wafer-scale silicon nitride cavities," Opt. Lett. **38**(11), 1760–1762 (2013).
19. M. Soltani, *Novel Integrated Silicon Nanophotonic Structures using Ultra-high Q Resonators* (Ph.D. Thesis. Georgia Institute of Technology, 2009).
20. B. Min, T. J. Kippenberg, L. Yang, K. J. Vahala, J. Kalkman, and A. Polman, "Erbium-implanted high-*Q* silica toroidal microcavity laser on a silicon chip," Phys. Rev. A **70**(3), 033803 (2004).
21. J. Hu, X. Sun, A. Agarwal, and L. C. Kimerling, "Design guidelines for optical resonator biochemical sensors," J. Opt. Soc. Am. B **26**(5), 1032–1041 (2009).
22. M. R. Watts, J. Sun, E. Timurdogan, E. Shah Hosseini, C. Sorace-agaskar, A. Yaacobi, Z. Su, M. Moresco, Purnawirman, J. D. B. Bradley, G. Leake, T. N. Adam, and D. Coolbaugh, "Very large scale integrated photonics," in *CLEO: Science and Innovations 2014*, OSA Technical Digest Series (Optical Society of America, 2014), paper SM4O.4.

1. Introduction

Optical microcavities are widely studied for their unique physical properties, including their small size, strong light-matter interactions, distinctive resonance spectra, and their important applications in photonic microsystems [1,2]. In optical microcavities with high quality factor (Q factor) the light is confined to small dimensions and resonates in the cavity for long periods with minimal loss leading to sharp resonances and high performance devices. Such resonators are particularly useful for quantum information systems [3], compact nonlinear optical devices [4], sensors [5] and ultra-low-threshold microlasers [6].

In silicon photonic microsystems, resonator-based devices perform important circuit functions, including filtering, switching, buffering, modulation and detection [7]. However, for compatibility with CMOS foundries, silicon photonic devices are typically limited to a handful of materials, including silicon itself, silicon nitride, silicon dioxide and germanium. While significant advances in silicon nanofabrication have led to high-Q-factor CMOS-compatible resonators [8–10], the limited selection of materials can limit the performance of or prevent entirely the implementation of certain types of integrated optical devices on a silicon platform. For example, low rare earth solubilities in the aforementioned materials preclude efficient rare-earth-doped devices such as lasers and amplifiers. Non-standard materials must be introduced by post processing methods which are typically difficult to incorporate into the layout of the silicon chip.

Over the last several years ultra-high-Q microcavities have been developed which can be integrated onto silicon chips and have shown extremely high performance in a number of resonator formats, such as microtoroids and microdisks [11]. However, because they are raised on the chip surface, such cavities have typically required an off-chip fiber for coupling

Optics EXPRESS

light to and from the cavity. Recently, promising results have shown that ultra-high-Q silica microcavities can be integrated with silicon nitride waveguides, which is a significant step towards their integration within on-chip microsystems [12]. In [13], we demonstrated a new type of micro-trench cavity, which has the advantages that it uses all silicon-photonics-compatible processing steps, is embedded in a silica cladding for robust form factor, has a nano-scale defined microcavity-waveguide gap for finely controlled and stable coupling, and can in principle accept any sputtered material as the resonator medium. Using this design we have demonstrated low threshold Yb-, Er- and Tm-doped aluminum oxide microlasers emitting at 1.0, 1.5 and 1.9 µm, respectively [13–15] and an athermal microcavity design using sputtered titanium dioxide as the resonator medium [16]. In [13] we reported Q factors of up to 5.7×10^5 at 1550 nm in undoped cavities, but we did not describe their design in detail or optimize their performance.

Here, we report in detail the design and properties of aluminum oxide micro-trench resonators co-integrated with silicon nitride waveguides on silicon. We compare the theoretical Q factors to those extracted from experimental transmission measurements at near infrared wavelengths. We show high Q factors of $> 10^6$ in such micro-trench cavities. These results serve as a basis for optimizing micro-trench cavities for a wide range of potential applications, including on-chip lasers, nonlinear optical devices and sensors, and can be applied to other microcavity materials systems towards their integration in silicon photonic microsystems.

2. Silicon-Photonics-Compatible Microcavity Design and Fabrication

Figure 1 shows the aluminum oxide micro-trench cavity fabrication process. The processing steps are similar to those described in [13–15], but repeated here for clarity and to avoid confusion with small design differences. We fabricated the microcavity chips using a 300-mm CMOS foundry with a 65-nm technology node. We first deposited a 6-µm-thick (plasma-enhanced chemical-vapor deposition) PECVD oxide layer on top of a silicon wafer and then deposited a 200-nm-thick PECVD Si_3N_4 film (nitride 1). The nitride 1 layer was then patterned to form the bottom piece of the Si_3N_4 waveguides. After this step, a layer of PECVD SiO_2 was deposited and chemical-mechanical planarized (CMPed) to leave a 100-nm-thick oxide on top of nitride 1. On top of the oxide layer, another layer of 200-nm-thick PECVD Si_3N_4 (nitride 2) was deposited and patterned, which was followed by a thick (~5 µm) SiO_2 deposition and planarization. The lateral alignment tolerance between the first and second patterned silicon nitride layers is ± 0.05 µm. The SiO_2 layer was then etched using reactive ion etching (RIE) to form the microcavity trenches using nitride 2 as an etch-stop layer and coated with a 100-nm-thick SiO_2 layer. Deep trenches were then etched for edge-coupling and the wafer was diced into individual chips. The above steps were all completed in the CMOS foundry. A ~1-µm-thick low-loss Al_2O_3 layer was then deposited onto the chips via reactive sputtering [17] to form the microcavities. Due to the angled configuration of the sputtering guns relative to the substrate in the sputtering system, Al_2O_3 was deposited conformally both inside the trench and on the sidewall (as shown in Fig. 1.vii). Due to the rotation of the sample holder and sputtering source angle, the film thickness on the trench wall is thinner than that on the bottom of the trench.

A schematic of a micro-trench cavity is shown in Fig. 2(a). It consists of a bus waveguide made of two nitride layers and a deep trench filled with Al_2O_3. To obtain an accurate profile of the resulting microcavity structure, we first deposited a layer of platinum (Pt) on the microcavity sample and then cut it along the black dotted line indicated in Fig. 2(a) using a focused ion beam (FIB). The layer of Pt is deposited on the chip before FIB cutting of the cross section as a protective layer and is not a part of the cavity design. The resulting cross-sectional scanning-electron-micrograph (SEM) image of the microcavity is shown in Fig. 2(b). The trench has a depth of around 5.2µm and a sidewall angle of ~85°. The image was taken with a sample tilt of 52° to the horizontal plane. Taking the tilt angle into account, we

calculated the ratio between the Al_2O_3 film thickness on the sidewall and the total deposited film thickness (measured away from the edge of the trench, defined as T in Fig. 2(b)) to be 0.44. A magnified view of the area enclosed in the red box in Fig. 2(b) is shown in Fig. 2(c). The bus waveguide is composed of two Si_3N_4 pieces. The width of the bus waveguide can be varied to phase-match to the resonant mode inside the cavity. The image also shows that a small ~250-nm-wide Si_3N_4 (nitride 2) piece exists adjacent to the SiO_2 trench as a result of the microcavity trench etching process.

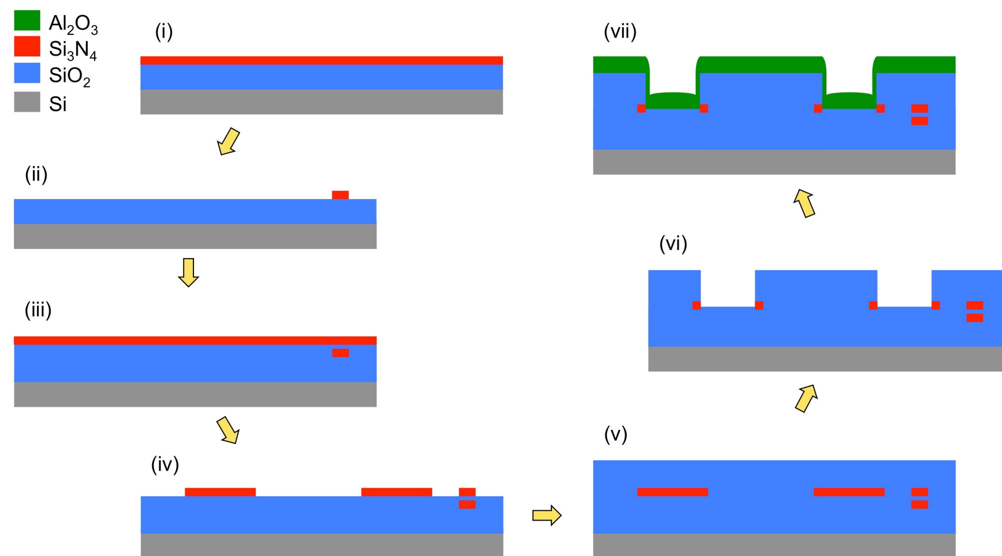

Fig. 1. Aluminum oxide micro-trench cavity fabrication process: (i) PECVD deposition and (ii) patterning of a 200-nm-thick Si_3N_4 film on a 6-µm-thick PECVD SiO_2 lower cladding layer on silicon; (iii) deposition and planarization of a PECVD SiO_2 layer to a height of 100 nm above the first Si_3N_4 layer and deposition of a second 200-nm-thick Si_3N_4 film; (iv) patterning of the second Si_3N_4 film; (v) deposition and planarization of a ~5-µm-thick SiO_2 top cladding; (vi) definition of the micro-trench into the SiO_2 cladding using RIE and the second Si_3N_4 layer as an etch stop followed by deposition of a 100-nm-thick SiO_2 layer; and (vii) deposition of a ~1-µm thick Al_2O_3 layer by reactive sputtering. Steps i–vi are completed in a silicon foundry, while step vii is carried out as a post-processing step.

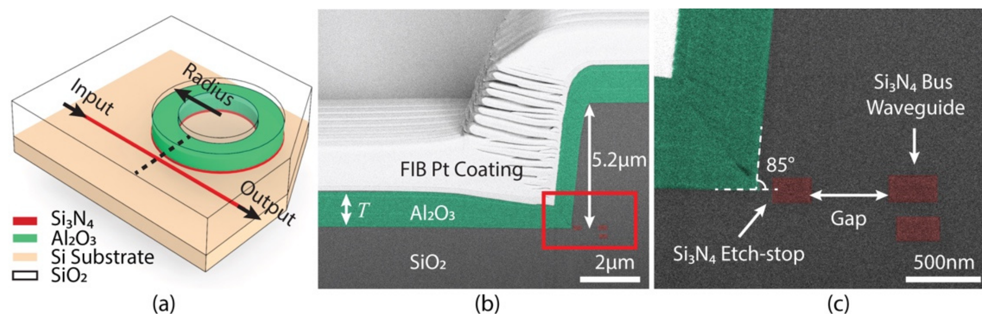

Fig. 2. (a) Schematic of a micro-trench cavity. (b) Cross-sectional SEM image taken along the dotted line in (a). The Pt coating is used as a protective layer during the FIB cutting of the chip and is not a part of the cavity design. (c) Magnified image of the cross-section (marked by the red rectangle in (b)) showing the trench angle, silicon nitride waveguide and gap.

We first characterized the refractive index of the Al_2O_3 film using a prism coupling system for a wide range of wavelengths and fitted the data to a Cauchy curve. The refractive indices of Al_2O_3 are shown in Fig. 3(a). The Al_2O_3 index at a wavelength of 1600 nm is around 1.65, which is higher than SiO_2. The index contrast allows the microcavity to support

Research Article Vol. 26, No. 9 | 30 Apr 2018 | OPTICS EXPRESS 11165
Optics EXPRESS

resonant modes having either transverse-electric- (TE-) or transverse-magnetic- (TM-) like polarization. Examples of the calculated electric field in the x direction (Ex-field) of a TE-like mode and electric field in the y direction (Ey-field) of a TM-like mode formed inside this type of microcavity are shown in Figs. 3(b) and 3(c), respectively. We note that the x, y and z directions in the figure are in the lateral, vertical and propagation directions, respectively. The modes were determined using a finite-element method modesolver. To optimize coupling to the modes supported in the resonator, it is crucial to determine their effective index. For bend modes in microcavities, their mode profiles will vary slowly with the change of the cavity radius when the cavity radius is relatively large. In Figs. 3(d) and 3(e), we show the effective indices for TE- and TM-like modes of a 100-µm-radius cavity for different wavelengths and thicknesses, where the effective indices are defined as

$$n_{\text{eff}} = \frac{m\lambda}{2\pi R}, \tag{1}$$

where m is the order of the mode, λ denotes the resonant wavelength, and R is defined as the outer radius of the cavity. This definition serves as an approximation that provides a close representation of a resonant mode in a relatively large-radius cavity. It can also serve as a good design reference even for small radii.

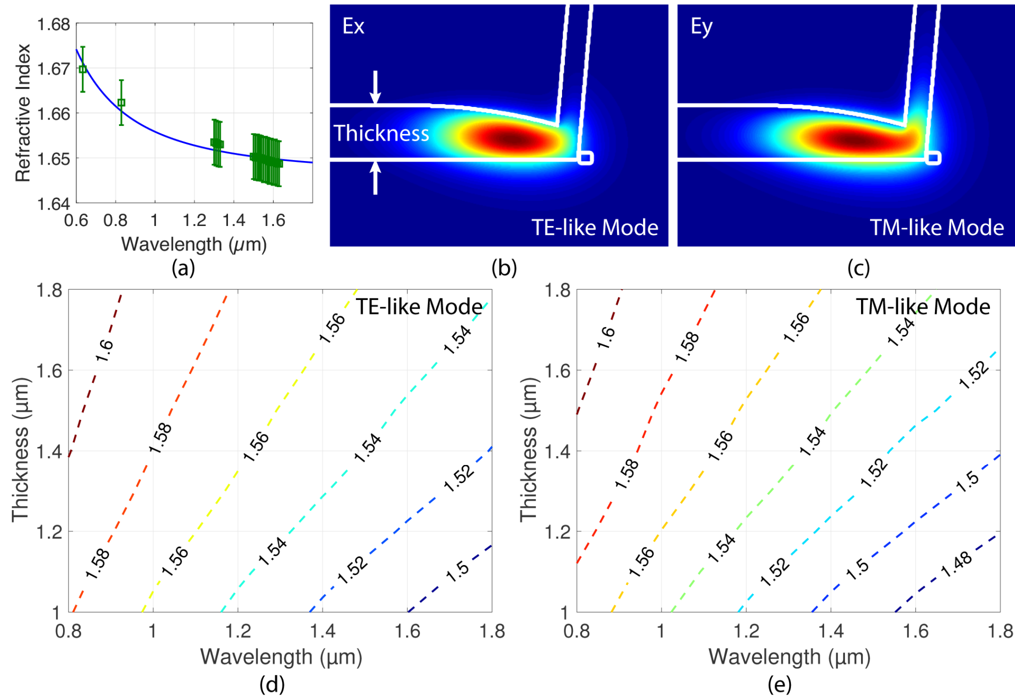

Fig. 3. (a) Measured refractive index of the amorphous Al_2O_3 film vs. wavelength. (b) Ex-field of the TE-like fundamental mode of the micro-trench cavity. (c) Ey-field of the TM-like fundamental mode of the micro-trench cavity. (d) Effective indices of the TE-like mode for different wavelengths and film thickness. (e) Effective indices of the TM-like mode for different wavelengths and film thickness.

For microcavity applications such as nonlinear optical devices and lasers where strong light-matter interactions are required, the cavity modes must have large intensity overlap, γ, with the resonator medium. In order to quantify this property, which we refer to as the confinement factor, we use the same definition as in Ref [18]:

Optics EXPRESS

$$\gamma = \frac{\int_{Al_2O_3} IdA}{\int_{\infty} IdA}, \qquad (2)$$

where the subscript Al_2O_3 denotes integration regions overlapping with the Al_2O_3 film, I is the optical intensity, and A is the area. Figure 4 shows the calculated confinement factors of TE- and TM-like modes for different Al_2O_3 thicknesses and radii at wavelengths of 980 and 1550 nm. We observe that a thicker film, in general, provides a higher confinement factor, and is therefore more favorable when considering, for example, the design of rare-earth-doped Al_2O_3 micro-trench cavity lasers. However, to optimize the performance of microcavity lasers and other devices, high confinement factors alone for both signal and pump modes are not enough. Other factors such as the passive loss of the cavity, pump and signal mode coupling from and to the Si_3N_4 waveguide, and signal/pump mode overlap are also crucial for achieving good device performance. For other devices, such as sensors, it might be critical to increase the intensity overlap with the region above the Al_2O_3 film, requiring a thinner film.

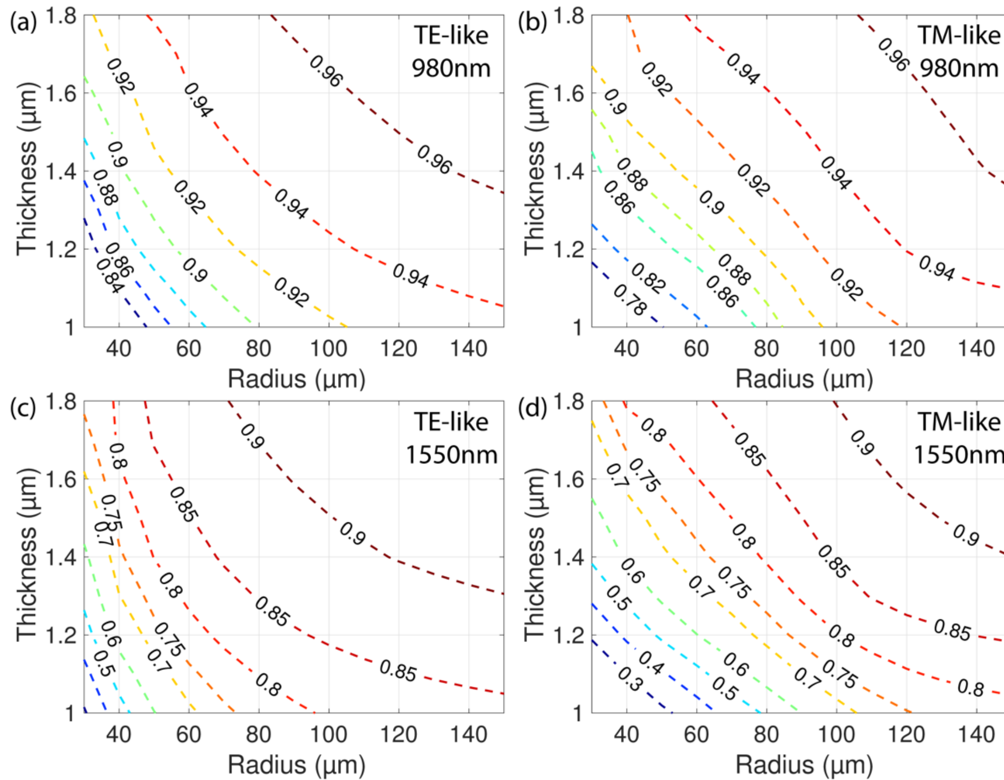

Fig. 4. Mode intensity overlap with Al_2O_3 for the (a) TE-like mode at 980nm, (b) TM-like mode at 980nm, (c) TE-like mode at 1550nm, and (d) TM-like mode at 1550nm for different microcavity radii and Al_2O_3 film thickness.

Since the trench-based Al_2O_3 microcavity design does not have an inner boundary, multiple higher order modes can also be supported. Therefore, the input light from the bus waveguide is able to excite multiple modes within the cavity at the same time [13,15]. To efficiently couple the pump light into a particular mode, the bus waveguide needs to be approximately phase-matched to the desired mode. We use two silicon nitride layers (nitride 1 and nitride 2) to form the bus waveguide. The double-layer waveguide can provide a highly confined mode to enable a small bend radius for waveguide routing while avoiding the greater

Optics EXPRESS

defects present in thick PECVD nitride films. It also enables a wider range of effective indices for phase matching to the resonator modes. The measured refractive indices of the PECVD Si_3N_4 film for different wavelengths are shown in Fig. 5(a). Typical TE-like and TM-like modes supported by the double-layer Si_3N_4 waveguide are shown in Figs. 5(b) and 5(c), respectively, while the effective indices for both modes for different wavelengths and waveguide widths are displayed in Figs. 5(d) and 5(e), respectively. By matching the effective index of the bus waveguide mode extracted from Fig. 5(d) or Fig. 5(e) with the effective index of the resonant mode from Fig. 3(d) or Fig. 3(e) for a particular polarization, wavelength, and film thickness, we are able to select a suitable bus waveguide width to allow for efficient coupling to the desired mode.

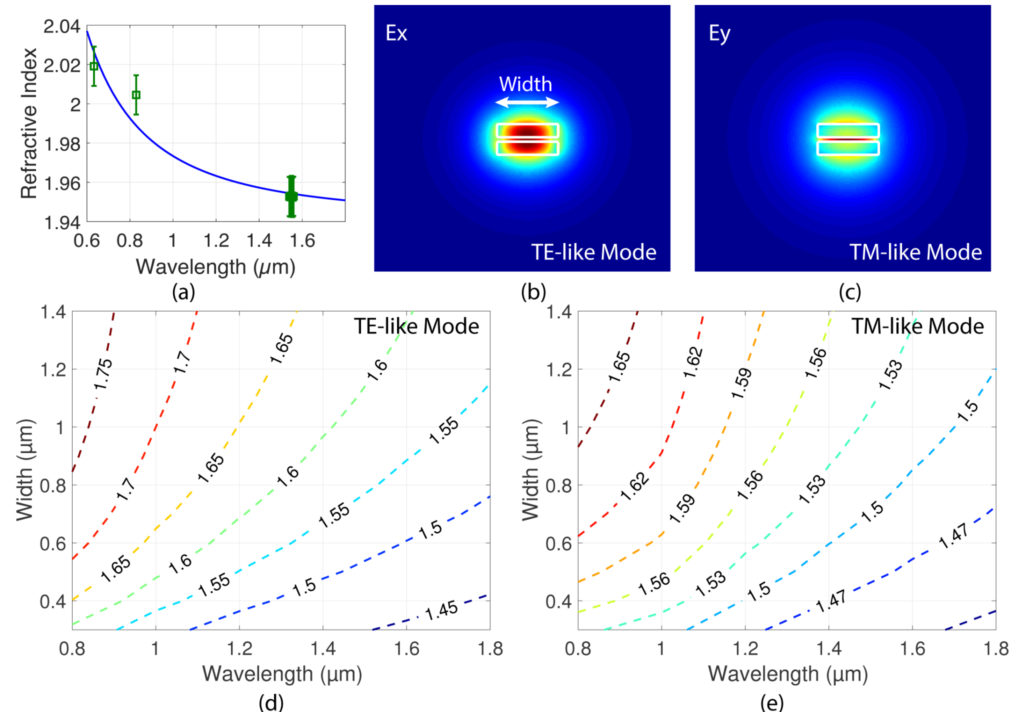

Fig. 5. (a) Measured refractive indices of the PECVD Si_3N_4 film vs. wavelength. (b) Ex-field of the TE-like mode and (c) Ey-field of the TM-like mode of the double nitride waveguide. (d) Effective indices of the TE-like mode and (e) effective indices of the TM-like mode for different wavelengths and waveguide widths.

3. Experimental Results

Optimizing the Q factor of optical microcavities is critical in order to build high performance devices. For example, since rare-earth-ion-doped glass has a relatively lower gain than III-V materials, in order to realize a laser using the microcavity design, achieving low loss and a high-intrinsic-Q-factor microcavity becomes the first priority. To analyze the loss within the cavity, we fabricated a set of devices with varying bus waveguide widths, coupling gap sizes, bending radii and Al_2O_3 film thicknesses. We measured the devices with high-resolution (0.1-pm step size) tunable lasers around 980, 1300, 1480, 1550, and 1610 nm wavelengths. The input light polarization was controlled with an external polarization controller. Inverse-taper silicon nitride waveguide couplers with 100-nm tip width for wavelengths around 980 nm and 300-nm tip width for the wavelength range 1300–1610 nm were used for efficient fiber-chip coupling. It was found that TM-polarized light couples better than TE-polarized light and the power level difference provided us an effective way to distinguish the transmission spectra for the two polarizations. For each wavelength, a set of devices with different coupling gaps

were fabricated to cover the regime where the microcavity is under-coupled. The transmission spectra were then fitted to the coupled-mode-theory model to extract the experimental extrinsic (coupling) and intrinsic Q factors [19].

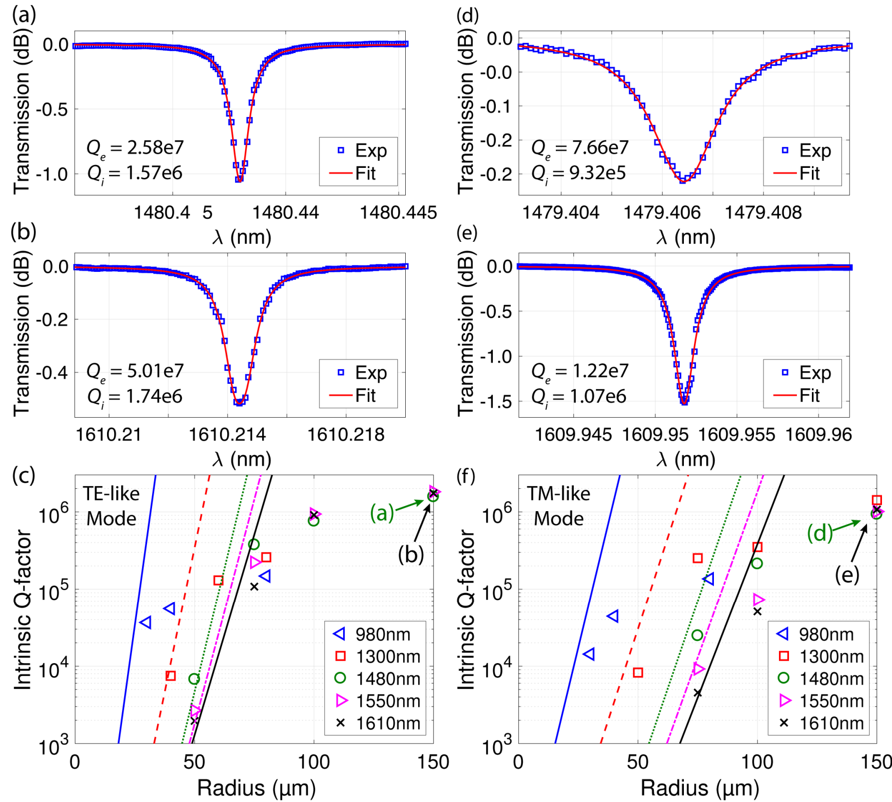

Fig. 6. Transmission spectra and Q factors measured for micro-trench cavities with a 1.16-µm-thick Al_2O_3 film. (a) (b) Sample transmission spectra for a 150-µm-radius cavity measured at 1480 nm and 1610 nm wavelength with TE-polarized inputs. (c) Measured (points) and calculated (lines) intrinsic Q factors for different radii and wavelength ranges for TE-polarized modes. The calculated Q factors were determined using a finite-difference modesolver. (d) (e) Sample transmission spectra for a 150-µm-radius cavity measured at 1480 nm and 1610 nm wavelength with TM-polarized inputs. (f) Measured (points) and calculated (lines) intrinsic Q factors for different radii and wavelength ranges for TM-polarized modes.

We first measured a set of devices with a film thickness of 1.16 µm. Examples of the measured transmission spectra for a 150-µm-radius cavity with TE-polarized input at wavelengths of 1480 and 1610 nm are shown in Figs. 6(a) and 6(b). We demonstrate that the cavity can support a mode with a Q factor > 10^6. Intrinsic Q factors for different radii and wavelengths with TE-polarized input are summarized in Fig. 6(c). The lines on the plots are the Q factors calculated using a finite-difference bend mode solver under the assumption that only radiation loss exists in the cavity. The measured Q factors match the simulated ones for small radii where radiation loss is the dominant loss mechanism in the cavity. We also observe that the intrinsic Q factors increase slowly with the expansion of the cavity size for regions where the radiation loss is negligible. The increase can be explained by the overlap between the resonant mode and the trench wall roughness of the cavity. Increasing radius shifts the resonant modes of the cavity inward, leading to less optical intensity overlap with the trench sidewall. Therefore, the intrinsic Q factors continue to increase for large radii. We also investigated TM-polarized modes in the cavity. Sample transmission spectra for a 150-µm-radius cavity with TM-polarized input at wavelengths of 1480 and 1610 nm are shown in

Optics EXPRESS

Figs. 6(d) and 6(e), respectively. Similarly, intrinsic Q factors for different radii and wavelengths with TM-polarized input are summarized in Fig. 6(f). We observe that TM-like cavity modes show relatively lower Q factors than those of TE-like modes. This difference can be explained by the lower confinement and larger mode overlap with the trench sidewall for the TM-like modes.

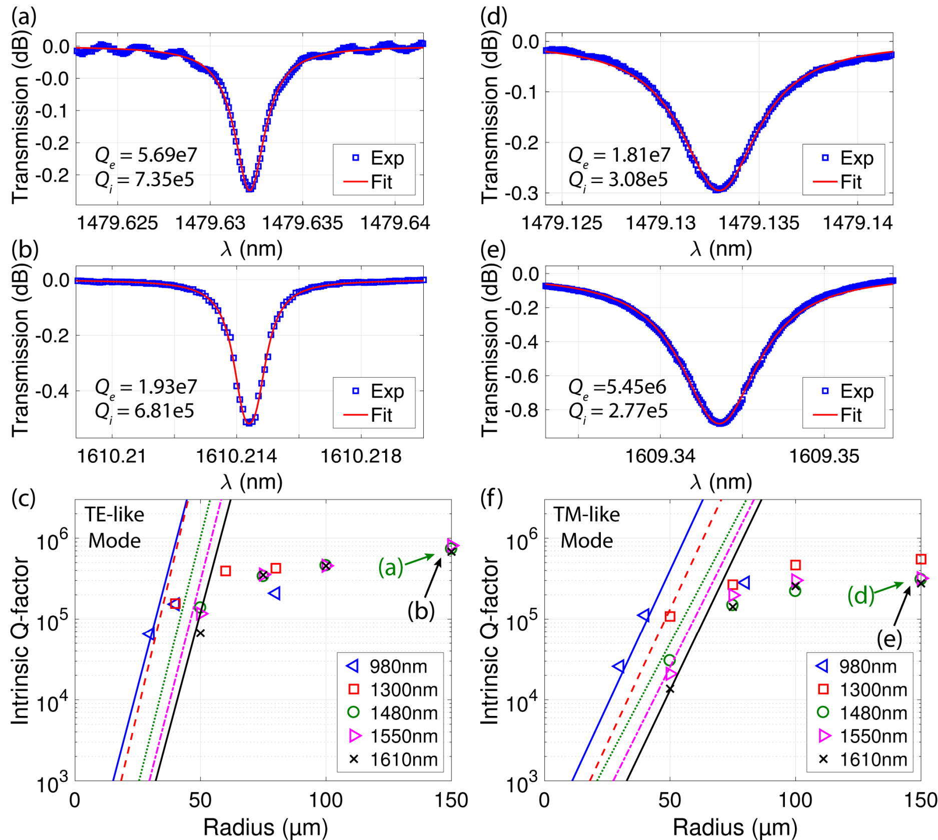

Fig. 7. Transmission spectra and Q factors measured for micro-trench cavities with a 1.58-μm-thick Al_2O_3 film. (a) (b) Sample transmission spectra for a 150-μm-radius cavity measured at 1480 nm and 1610 nm wavelength with TE-polarized inputs. (c) Measured (points) and calculated (lines) intrinsic Q factors for different radii and wavelength ranges for TE-polarized modes. The calculated Q factors were determined using a finite-difference modesolver. (d) (e) Sample transmission spectra for a 150-μm-radius cavity measured at 1480 nm and 1610 nm wavelength with TM-polarized inputs. (f) Measured (points) and calculated (lines) intrinsic Q factors for different radii and wavelength ranges for TM-polarized modes.

We also fabricated and characterized another set of devices with an Al_2O_3 film thickness of 1.58 μm. Examples of the measured transmission spectra for a 150-μm-radius cavity with TE- and TM-polarized inputs and wavelengths of 1480 and 1610 nm are shown in Figs. 7(a), 7(b), 7(d), and 7(e). Compared to the Q factors of the same device but with a thinner film, a thicker film provides a relatively lower intrinsic Q factor for 150-μm-radius devices. The difference is caused by an increased mode overlap with the trench sidewall roughness as a result of mode size expansion. Summaries of the intrinsic Q factors of TE- and TM-like modes for different radii and wavelengths for the 1.58-μm-thick film are shown in Figs. 7(c) and 7(f). We observe that for a small-radius device such as the 50-μm-radius device where the intrinsic Q factor is limited by radiation loss, the thicker film provides better intrinsic Q factors than that of the thinner film because of the increase in mode confinement. Therefore,

to realize compact and high performance microcavity devices, a thicker Al_2O_3 film is preferred.

4. Discussion

For our current design and fabrication technique, we have achieved a maximum *Q* factor of 1.7 million at 1610 nm for devices with a 150-µm radius. However, making this microcavity design more compact while maintaining a *Q* factor on the scale of 1e6 requires further optimization of the trench sidewall roughness. For our current fabrication process, the microcavity trench is fabricated using dry etching with a relatively low-resolution mask. To make the trench wall smoother, a fast HF wet etch of the device would be helpful. Other factors limiting the *Q* factor could be the Al_2O_3 film quality, defects at the SiO_2-Al_2O_3 interface or grain boundaries in the Al_2O_3 film such as the one visible in the corner of the micro-trench cavity in Fig. 3(c). Further investigation will lead to a better understanding if the *Q* factor is bend-loss, SiO_2-sidewall-quality or Al_2O_3-film-quality limited or a combination thereof.

Another key structural parameter that can be improved is the trench wall angle. In the devices presented above, the trench wall angle is estimated to be around 85°. For a small radius device, the resonant mode is pushed towards the trench wall, and the film deposited on the trench wall starts acting as a leaking channel. Through optimizing the trench wall angle towards 90°, a more confined mode for a small-radius device can be achieved, making it possible to further reduce the cavity footprint while maintaining a relatively high intrinsic *Q* factor.

Importantly, we have demonstrated a maximum *Q* factor more than twice as high as that shown in [13], moving micro-trench cavities into a regime ($Q > 10^6$) where they can be applied in high performance devices such as ultra-low threshold lasers [20], highly efficient sensors [21] and Kerr combs [4]. Future implementation of micro-trench cavities on a full silicon photonics platform incorporating silicon nitride layers [22] can lead to their application in silicon photonic microsystems, including as light sources, reservoirs for sensing, and nonlinear optical devices.

5. Conclusion

To summarize, we have demonstrated a straightforward approach to create an on-chip high-*Q*-factor Al_2O_3 microcavity with coupling achieved via a co-integrated silicon nitride waveguide. We analyzed both the theoretical and experimental micro-trench resonator and bus waveguide properties. We achieved a maximum *Q* factor on the scale of $> 10^6$ for this type of cavity, making it possible for further development of high performance integrated optical micro-trench cavity devices. The micro-trench cavity design is robust, silicon-photonics-compatible, enables precise and stable coupling via the integrated waveguide and potentially allows for the implementation of a wide variety of microresonator materials into a silicon photonics platform.

Funding

Defense Advanced Research Projects Agency (DARPA) (HR0011-12-2-0007, HR0011-15-C-0056); McMaster University Faculty of Engineering Startup Grant; Natural Sciences and Engineering Research Council of Canada (NSERC) (RGPIN-2017-06423).

Acknowledgments

The authors would like to acknowledge Gary Riggott and Kurt Broderick for assistance with aluminum oxide thin film deosition. N. Li acknowledges a fellowship from the Agency of Science, Technology and Research (A*STAR), Singapore.

18.62.22.143 {ts '2018-05-25 14:11:06'}